doi:10.20944/preprints201907.0304.v1

Article

Elimination of Cypermethrin using Fe-TiO_2 nanoparticles supported on coconut palm spathe using a solar flat plate photoreactor

Ricardo Solano [1],* and Adriana Herrera [1]

[1] Nanomaterials and Computer aided process engineering Research Group, Chemical Engineering Program, Universidad de Cartagena; aherrerab2@unicartagena.edu.co

* Correspondence: rsolanop@unicartagena.edu.co; Tel.: +57-300-671-8267

Abstract: In this research, the photocatalytic degradation of cypermethrin using Fe-TiO_2 nanoparticles supported in a biomaterial was evaluated. The nanoparticles of TiO_2 were synthesized by the green chemistry method assisted by ultrasound and doped by chemical impregnation using molar ratios Fe:Ti of 0, 0.05, 0.075 and 0.1, to make efficient use of direct sunlight (λ>310 nm). All nanoparticles were immobilized on the surface of spathe of coconut palm (*Cocos nucifera*). The degradation was carried out at room temperature and natural pH in a flat plate solar reactor, on which the composite material was subjected. The concentration of cypermethrin was determined after 12000 J/m^2 of accumulated radiation from GC-MS and the resulting material was characterized by Scanning electron microscopy (SEM), Transmission electron microscopy (TEM) image and selected area electron diffraction (SAED), Fourier transform infrared spectroscopy (FTIR), UV-Vis spectrophotometry of diffuse reflectance and BET surface area BET surface area. The best results were achieved with the use of Degussa TiO_2 P-25, Fe:Ti=0 and Fe:Ti=0.05 in suspension, with percentages of degradation of cypermethrin of 99.84, 99.62, and 100%, respectively. However, the materials supported on the biomaterial of coconut, they allowed to reach degradation percentages higher than 80% with the advantage that it minimizes operating costs, since they are not necessary filtering or centrifuging processes to separate the catalyst.

Keywords: Cypermethrin; green chemistry; photocatalysis; sunlight; flat plate

1. Introduction

The current paradigm of the intensification of pest control in agriculture has increased the demand for pesticides, because these have become fundamental tools in the productivity of the agroindustrial sector [1–5]. This industry generates approximately 150 million tons of wastewater during the year worldwide [6], mainly by the use of herbicides, fungicides and insecticides, approximately 3.3x10^6 T/year worldwide, of which 0.42x10^6 T/year are consumed in Europe (data 2010-2014 of FAOSTAT) [7]. This wastewater shows very different characteristics, due to the diversity of pesticides (herbicides, insecticides, fungicides, rodenticides, nematicides, microbicides and regulators of plant and insect growth) that can be found in concentrations of up to 500 mg/L [6,8]. The excessive amount of pesticide residues in the soil, surface water and groundwater causes serious contamination of soil and water, due to its high toxicity and persistence, which has been declared as priority pollutants by the Environmental Protection Agency of the United States. United States (EPA) [9–11]. On the other hand, European legislation for drinking water sets a limit of 0.1 μg/L for a single active ingredient of pesticide and 0.5 μg/L for the sum of all the individual active substances detected [6]. In Colombia Resolution No. 2115 of June 22, 2007 establishes that the maximum permissible limit value for the active ingredients of pesticides of toxicological category II [12] is 0.1 mg/L [13]. Cypermethrin (Class II, moderately dangerous) causes human health problems related to immunosuppression, hormonal alteration, diminished intelligence, reproductive anomalies and cancer. In the studies carried out in this area, only 0.1% of the pesticide used reaches the target pest and 99.9% is dispersed in the environment through routes such as runoff and erosion, leaching, drainage and discharges of pesticide production plants [14].

In urban wastewater treatment plants, biological treatment does not eliminate polar, toxic or non-biodegradable contaminants, although it is adopted as the best available technology. To comply with strict environmental laws, significant efforts are being made to develop effective, rational and affordable wastewater treatment strategies, and improvements in processes that can easily destroy all bio-recalcitrant organic pollutants, minimizing their accumulation [15]. Advanced oxidation processes (AOPs) are characterized by the "insitu" production of hydroxyl radicals (OH●), which are capable of oxidizing and mineralizing any organic molecule, producing CO_2, H_2O and inorganic ions. Due to the reactivity of the hydroxyl radicals, its attack is non-selective, which is useful for the treatment of wastewater containing different pollutants. AOPs can be made with solar irradiation, since the sun (a source of clean renewable energy) provides photons with the wavelength required for these processes [8,9,16–18]. Heterogeneous Photocatalysis is an advanced oxidation technology for the degradation of persistent organic pollutants, such as pesticides, which produces byproducts that are more biodegradable than the original compounds. TiO_2 is the most common photocatalyst in this process when applying UV/UV-vis. Some strategies to expand the photo-response of TiO_2 in the region of visible light is the doping of this material with non-metallic elements [19–21] , such as N, C, B, P and F, with noble metals such as Au and transition metals such as Cr, Fe, Ni, V, Mn, and Cu [22–27]. In the photocatalytic degradation of chlorpyrifos, a composite material of $CoFe_2O_4$-TiO_2/reduced graphene was used in a batch reactor under UV radiation, reaching a degradation efficiency of 95% for an initial concentration of 5 mg/L, pH 5.8, catalyst dose 0.6 g/L and 60 min of reaction [15,28,29]. In a similar study, the batch degradation of atrazine was evaluated using B-TiO_2 nanomaterials, with efficiencies close to 85% in the photocatalytic process [30]. Additionally, heterogeneous photocatalysis has been integrated with other advanced oxidation processes such as ozonation. The O_3/UV/TiO_2 treatment has been proposed for the elimination of cypermethrin, malathion and dichlorovos, by means of which 83% degradation percentage was obtained for cypermethrin [8,31]. In addition, a wide variety of common pesticides such as bromoxynil, diuron, o-phenylphenol, MCPA and terbuthylazine have been mineralized through heterogeneous photocatalysis using B-TiO_2 and Cs-TiO_2 catalysts, which exhibit degradation efficiencies greater than 75% for these pollutants [32,33].

In the present research the photocatalytic degradation of Cypermethrin was evaluated using Fe-TiO_2 nanoparticles in slurry and supported on coconut palm spathe (*Cocos nucifera*) in a flat plate solar reactor for a Cypermethrin initial content of 50 mg/L. The nanoparticles of TiO_2 were synthesized by the method of Green Chemistry assisted by ultrasound using aqueous extract of lemon grass (*Cymbopogon citratus*), obtained from Soxhlet extraction and modified with Fe^{+3} atoms by means of Chemical Impregnation, while the immobilization of the nanoparticles on Coconut palm spathe was carried out through the Doctor Blade technique. The concentration of cypermethrin was determined after 12000 J/m^2 of accumulated radiation from GC-MS, the powder materials was characterized by Transmission electron microscopy (TEM) image and selected area electron diffraction (SAED), Fourier transform infrared spectroscopy (FTIR), UV-Vis spectrophotometry of diffuse reflectance and BET surface area, while composite materials (coconut palm spathe/catalyst) were analyzed through Scanning electron microscopy (SEM).

2. Materials and Methods

2.1. Materials

Fresh lemongrass plant leaves (*Cymbopogon citratus*) were collected from Cartagena, Colombia. Titanium(IV) isopropoxide ($C_{12}H_{28}O_4Ti$) solution (95%) and Iron (III) chloride hexahydrate (98%

purity) were purchased from Alfa Aesar® and Panreac, respectively. All reactions were carried out using ACS Reagent chemicals.

2.2. Plant extract and green synthesis of Fe-TiO_2 nanoparticles

Lemongrass aqueous extract and TiO_2 nanoparticles using green chemistry were obtained through a previously reported procedure [34]. The lemongrass leaves were washed with griffin water. Then, they were dried for six hours in an air circulation oven at 60 °C (Esco Isotherm®, OFA 32-8) and crushed using a manual mill. The dried and crushed biomass (100 g) was placed in cloth bags, and subjected to a solvent extraction process using a Soxhlet extractor for 6 h in approximately 600 mL of distilled water [35,36]. The extract was stored in the refrigerator at 4 °C. Further, this extract was used to synthesize TiO_2 nanoparticles [37]. In a typical experiment, the reaction was carried out in a 250-mL beaker, which was introduced in an ultrasound processor (Ultrasonic processor, WiseClean WUC-A06H, 60 Hz). 20 mL of the precursor agent (Titanium isopropoxide) was added 100 mL of the aqueous extract of lemongrass contained in a burette, at a rate of 1 mL s^{-1}, additionally the reaction lasted approximately 30 minutes with constant agitation, making use of a stirring rod [22,37]. The nanoparticles were washed with 70 %vol ethanol and finally with distilled water, using separation by centrifugation (Universal Centrifuge PLC-012E) for 15 min at 5000 rpm. The synthesized titanium dioxide nanoparticles were calcined at 550 °C for 3 hours in a Thermo SCIENTIFIC FB1415M-1450 W-50/60 Hz muffle [16]. For wet impregnation, 1 g of TiO_2 and the amount of $FeCl_3{\cdot}6H_2O$ were weighed to obtain Fe^{3+}:Ti molar ratios of 0.05, 0.075 and 0.1 and dissolved in 20 mL of double distilled water with constant magnetic stirring for 1 h at 500 rpm. Then, the precipitate was washed with distilled water and separated by centrifugation for 15 minutes at 5000 rpm, repeating the process 3 times. Next, the precipitate was calcined at 350 °C for 3 h, and finally the catalyst was sieved in a 300 mesh [23,38].

2.3. Immobilization of Fe-TiO_2 nanoparticles on coconut palm spathe

The immobilization of the nanoparticles on spathe of coconut palm was carried out through the Doctor Blade technique using a water-based emulsion composed of styrene copolymer and 50% solids acrylic ester (RECOL ® CRYL) [39–43]. For this, 0.15 g of nanoparticles were dissolved in 4 g of emulsion, which was applied in thin film on a spathe surface of 10 cm x 10 cm.

2.4. Characterization

The micrographs of the composite materials were taken in SEM FEI Inspect™ S50. Investigation of particle morphology of Fe^{3+} doped and pure TiO_2 samples was performed on a JEM 2100HT JEOL transmission electron microscope (TEM) provided with 200 kV emission gun, beam current of 108.6 µA, and equipped with diffraction mode (camera length of 300 mm) for selected area electron diffraction (SAED). The samples were prepared by ultrasonic dispersing of the powders as slurry in 2-propanol and deposited in TEM grids. FT-IR spectroscopy was made on using a IRAffinity-1 Fourier Transform Infrared Spectrophotometer SHIMADZU in the spectral range of 400 and 4000 cm^{-1}. The spectra of the samples were collected by the KBr pellet technique. The sensibility of apparatus was 4 cm^{-1}. The specific surface area (BET method) was measured by nitrogen adsorption analysis at -196 °C using a Micromeritics ASAP 2020 Surface Area and Porosity analyzer. Prior to N_2 adsorption, the samples were out gassed at 300 °C for 2 hours in vacuum. Note: A 0.1 g of the catalyst sample. The UV–vis absorption studies of the photocatalysts were conducted on UV–vis diffuse reflectance spectrophotometer (Thermo Scientific EVOLUTION-600), with $BaSO_4$ as reference.

2.5. Solar photocatalysis experiment

The experiment was carried out in a lab scale pilot plant in Cartagena, Colombia (latitude 10° 25′ 30′′ N, longitude 15° 32′ 25′′ W) using natural sunlight irradiation during July to September of 2018. Radiation were taken with a portable photoradiometer Delta Ohm HD 2102 with LP-UVB (300-600 nm) probe. The solar lab scale pilot used in this experiment is based on flat plate solar reactor (FPSR) technology (Figure 1). This small prototype consists of one photoreactor module (100 cm^2)

where the water flows directly from tube to flat plate and finally to the reservoir tank (1 L) and a centrifugal pump (12V DC, 0.7A, 1/2-inch suction/discharge diameter and 8 L/min maximum flow). Storage tank, flowmeter (Arduino flow sensor by effect hall YF-S401, Working Voltage: DC 5V-24V, Flow Rate Range: 0.3- 6L/min), pipes (1/4-inch), and fittings completed the installation. In photocatalysis assay, 250 mL of solution (50 mg/L of Cypermethrin) was prepared, this will be exposed to sunlight in the flat plate photocatalytic reactor without (photolysis test) and with addition of a catalyst (powder and composite) until it reaches a cumulative solar radiation value of 12000 J/m^2. For the molecular adsorption test, 250 mL (50 mg/L) were placed in contact with the synthesized composite or 0.15 g of Fe-TiO$_2$ (Fe: Ti = 0). The solution was maintained in constant recirculation at 1.3 L/min in a closed wooden box, taking samples at the beginning and after 120 min, separating the solution by centrifugation when this is required.

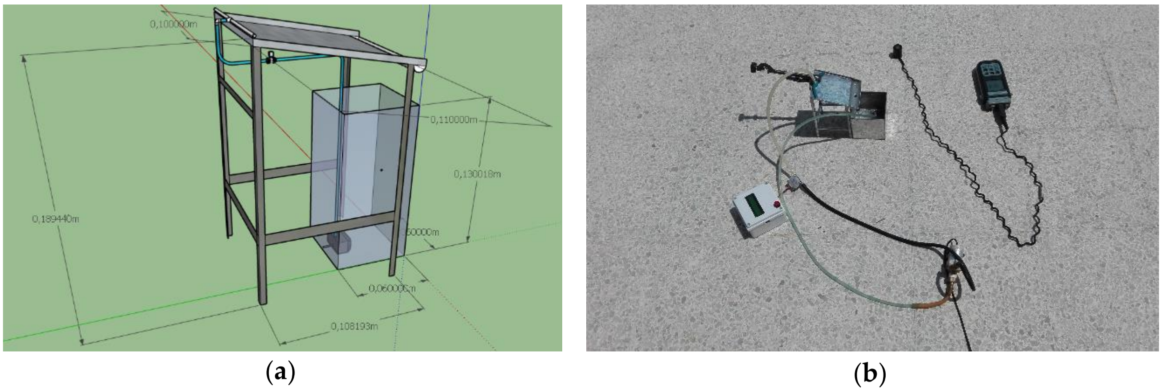

(**a**) (**b**)

Figure 1. flat plate solar reactor: (**a**) Design; (**b**) lab scale.

3. Results and Discussion

3.1. Characterization

3.1.1. Scanning electron micrographs (SEM)

Figure 2 shows the microscopy of Coconut palm spathe coated by Doctor Blade technique. Samples prepared with water-based emulsion composed of styrene copolymer and 50% solids acrylic ester (Figure 2a, 2b, 2c and 2d) present a rough non-homogeneous layer of TiO$_2$ or Fe-TiO$_2$ and some cracks are visible, similar to that reported by Mejía et al. [44].

3.1.2. FTIR spectroscopy

FTIR spectra were also recorded between the wave number of 400 and 4000 cm^{-1} for all the samples. The FTIR spectrum of all the samples is shown in Figure 3 for which nearly similar patterns were observed. The functional groups of the commercial catalyst (Evonik P-25) prepared TiO$_2$ and Fe-TiO$_2$ were determined using FTIR. The synthesized TiO$_2$ and Fe-TiO$_2$ absorption band at 3400 cm^{-1} can be assigned to the vibration of OH groups including the Ti-OH group. The band at 1620 cm^{-1} corresponds to the Fe-TiO$_2$ bond and H-O-H bending vibration of adsorbed water [16]. The absorption peak between 400 and 690 cm^{-1} corresponds to the Ti-O-Ti bond vibration and the symmetrical vibration of Fe-O-Fe bonds, for the case of doped nanomaterials. All four synthesized materials have high intensity of Ti-O-Ti bond, including the reference material (P-25) [45].

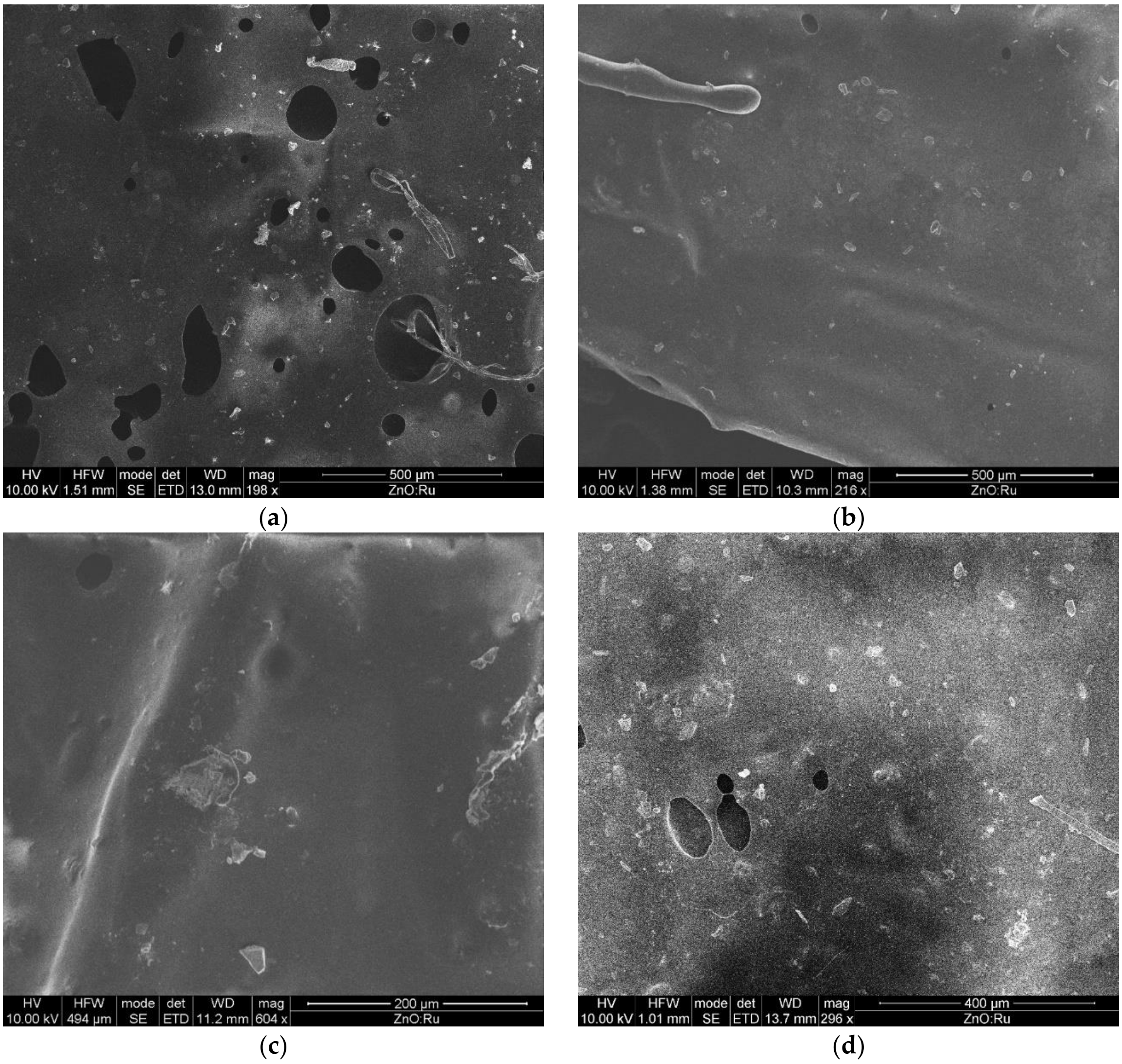

Figure 2. SEM micrograph of: (**a**) Fe:Ti=0/spathe; (**b**) Fe:Ti=0.05/spathe; (**c**) Fe:Ti=0.075/spathe; Fe:Ti=0.1/spathe.

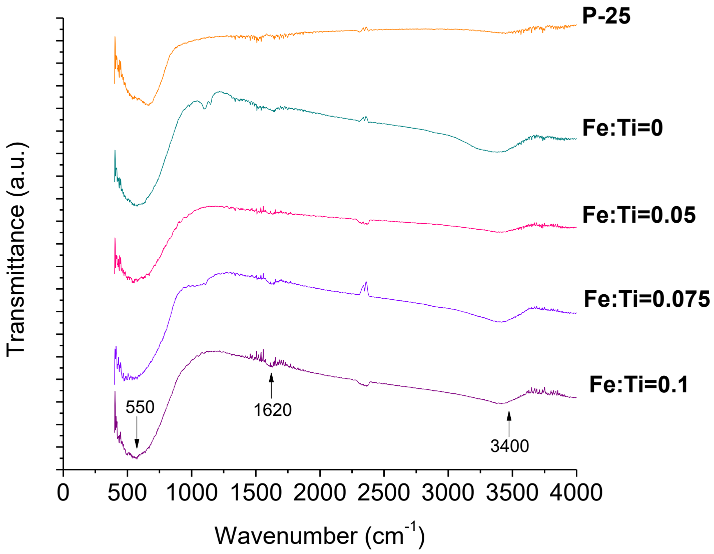

Figure 3. Typical FTIR spectra of as-prepared different Fe doped and bare TiO_2.

Preprints (www.preprints.org) | NOT PEER-REVIEWED | Posted: 26 July 2019 doi:10.20944/preprints201907.0304.v1

3.1.3. TEM and selected area electron diffraction analysis (SAED)

The surface morphology and particle size (size distribution) of the pure (Fe:Ti=0) and Fe-doped TiO_2 (Fe:Ti=0.1) photocatalyst were further analyzed by TEM, as shown in Figure 4a and Figure 4b, respectively. It is evident from these images that the synthesized nanoparticles were agglomerated, and their shapes were quasi-nanospheres. Also, it can be seen that particles have a small size but are perfectly crystalline in nature. The TEM results are in close agreement with the average crystallite size obtained from the XRD pattern. The average particle size increases for Fe:Ti=0.1 (15 nm ± 3.057) as compared to pure TiO_2 (13 nm ± 2.542), which is attributed to nanoparticles growth in the calcination process of the wet impregnation at 350 °C for 3 h. The SAED pattern for pure TiO_2 and Fe-TiO_2 (Fe:Ti=0.1) is shown in Figure 5a and Figure 5b, respectively. The lattice spacing was determined by using the Equation (1):

$$\frac{1}{d^2_{(hkl)}} = \frac{h^2 + k^2}{a^2} + \frac{l^2}{c^2} \qquad (1)$$

Where, h, k, l are the Miller indices and a and c are the lattice parameters, for a tetragonal structure, $a = 3.7852 = b \neq c = 9.5139$ and d_{hkl} is the lattice spacing value [46,47].

The structural information obtained from SAED pattern shows the polycrystalline nature of TiO_2 and Fe-TiO_2 nanoparticles (Fe:Ti=0.1), which is indicated by the (101), (103), (004), (200) and (105) plane of the anatase phase, similar to that reported by Ali et al. [48].

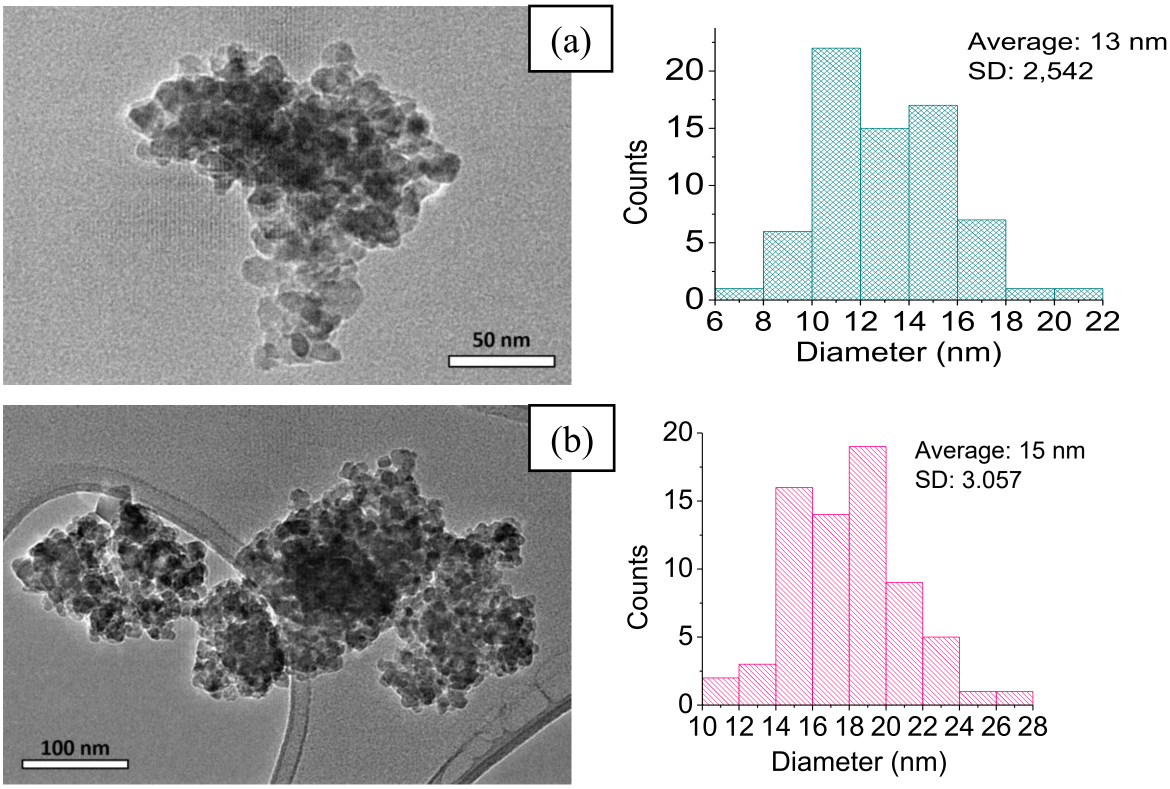

Figure 4. TEM image and particle size distribution of: (**a**) bare TiO_2; (**b**) Fe-TiO_2 (Fe:Ti=0.1).

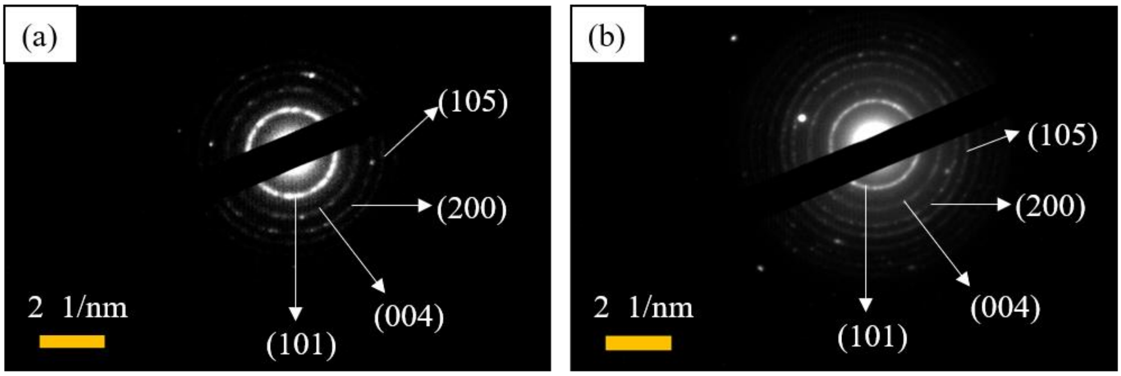

Figure 5. SAED pattern of: (**a**) Fe:Ti=0/spathe; (**b**) Fe:Ti=0.05/spathe; (**c**) Fe:Ti=0.075/spathe; Fe:Ti=0.1/spathe.

3.1.4. Optical property

The optical properties of TiO_2 and Fe-TiO_2 were separately detected by ultraviolet- visible diffuse reflection spectrometer (UV–Vis DRS). According to the Figure 6a, the absorption edge of the Fe-TiO_2 in comparison to undoped TiO_2 is extended greatly toward the visible light. The absorption edge is more extended to the visible light with the increasing of the Fe concentration, which is induced by the electron transition from Fe3d orbitals to TiO_2 conduction band (CB) [22]. Doping Fe^{3+} causes structural defects of crystal lattice to introduce impurity or defect energy level and induces the local states below the conduction band edge, then results in this redshift and narrows the band gap [23]. Although doping of the Fe ions in the TiO_2 does not modify the position of the valence band edge of the TiO_2, it introduces new energy levels (Fe^{3+}/Fe^{4+}) of the transition Fe ions into the band gap of the TiO_2 [49]. The direct band gap energy (Eg) was calculated using the following Tauc plot (Equation (2)), which derived assuming a direct transition between the edge of the valence band and conduction.

$$(\alpha h v)^{1/n} = A(hv - E_g) \tag{2}$$

Where hv is the photon energy, α is the absorption coefficient and A is an energy dependent constant and known as the band tailing parameter. Another constant is n, which is known as power factor of the transition mode of the materials. The values of n for direct, indirect, direct forbidden and indirect forbidden transitions are 1/2, 2, 3/2, and 3, respectively. The pure anatase and Degussa P25 TiO_2 used in this research are cosidered as direct band gap materials [50,51]. Therefore, the value of n was taken 1/2 to plot the graph $(\alpha hv)^2$ versus hv is shown in Figure 6b. Table 1 shows the results obtained for the band gap of pure and doped TiO_2.

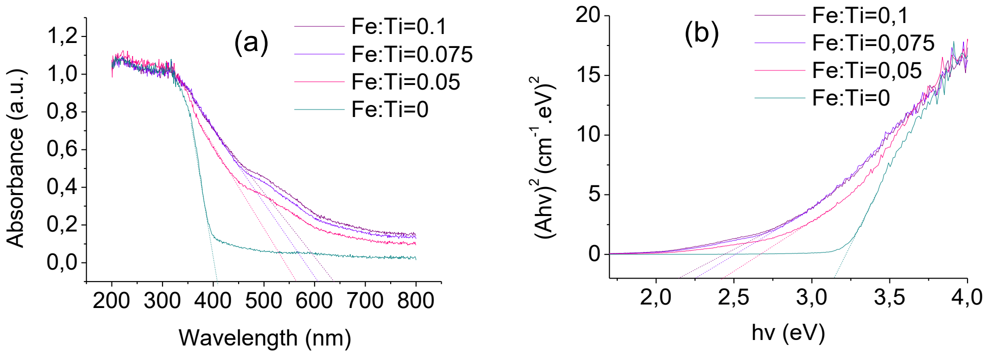

Figure 6. Optical property studies: (**a**) Typical UV–vis spectra of bare TiO_2 and Fe-TiO_2; (**b**) Tauc plot analysis of bare TiO_2 and Fe-TiO_2.

228 **Table 1.** The direct band gap energy (Eg) for pure and doped TiO_2.

Sample	Wavelength (nm)	Bandgap energy (eV)
P-25	-	3.1 [1]
Fe:Ti=0	407.27	3.14
Fe:Ti=0.05	563.76	2.42
Fe:Ti=0.075	606.76	2.25
Fe:Ti=0.1	636.31	2.14

229 [1] Reported by Hossain et al. [51].

230 3.1.5. Surface area and porosity analysis

231 N_2 physical adsorption-desorption studies were conducted to determine the surface area and 232 the pore distribution of the synthesized TiO_2 and Fe-TiO_2 samples. The isotherms and their relative 233 Barret-Joyner-Halender (BJH) pore size distributions obtained from the adsorption branch of the 234 isotherms of the catalysts are shown in Figure 7 and 8, respectively.

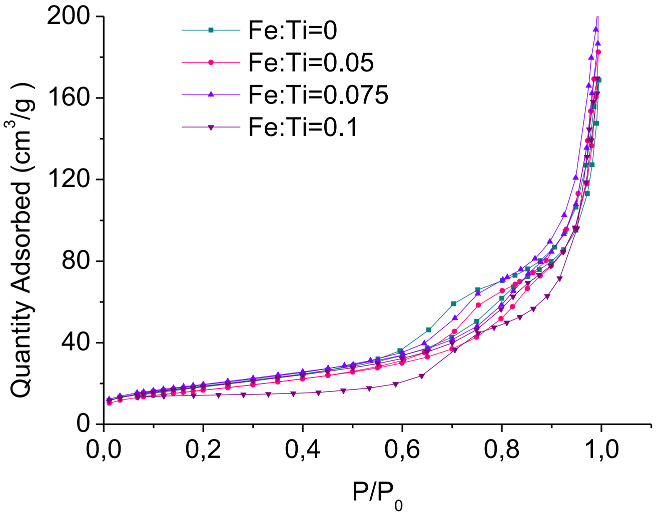

235

236 **Figure 7.** Nitrogen adsorption-desorption isotherms of bare TiO_2 and Fe-TiO_2.

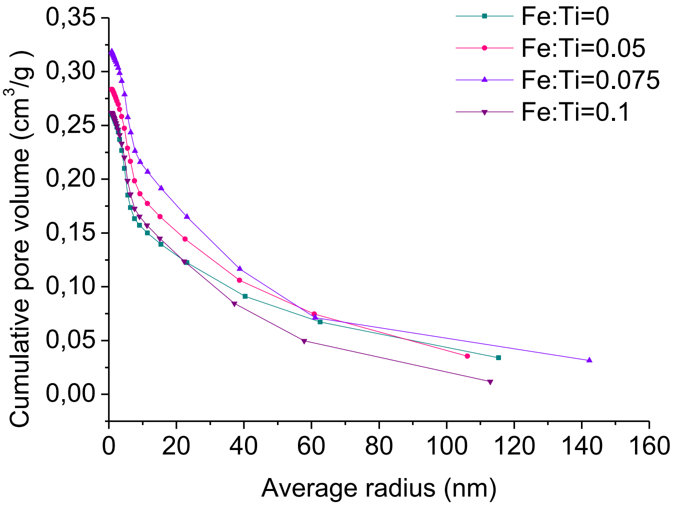

237

238 **Figure 8.** Cumulative pore volume from BJH adsorption isotherm.

In Figure 7, it was observed that the prepared TiO_2 and Fe-TiO_2 possess mesoporous surface as the isotherms are of Type IV and with typical H3 hysteresis loop according to the IUPAC convention, it indicates that TiO_2 sample contain non-rigid aggregates of plate-like or slit shaped pores with a contribution of micropores and mesopores [52–55]. Furthermore, Figure 8 shows broad pore size distributions, ranging from 1.7 to 280 nm, further confirming the existence of micropores, mesopores and macropores in TiO_2 and Fe-TiO_2 samples according to the Barret-Joyner-Halender (BJH) adsorption pore distribution [53]. Additionally, From BET data, the particle size, D (nm) was estimated using Equation (3) [56], assuming a spherical shape for particles, where S_{BET} refers to BET surface area (m^2/g) and ϱ refers to density of samples (g/cm^3) and V_{pore} is single point adsorption total pore volume of pores less than 2069,006 Å radius at P/P_0= 0,995. Table 2 summarizes the results obtained by Equation (3).

$$D = 6000(S_{BET} \times \rho)^{-1} \quad (3)$$

Table 2. Textural properties of pure TiO_2 and Fe-TiO_2 nanoparticles.

Sample	**S_{BET} (m^2/g)**	**V_{pore} (cm^3/g)**	**D (nm)**
Fe:Ti=0	64.4422	0.2610	21.0319
Fe:Ti=0.05	60.4994	0.2822	23.4455
Fe:Ti=0.075	70.5664	0.3192	20.1007
Fe:Ti=0.1	66.6617	0.2623	21.2781
Fe:Ti=0	64.4422	0.2610	21.0319

3.1. Solar photocatalytic degradation of Cypermethrin

Results obtained for the photocatalytic degradation of Cypermethrin using nanomaterials suspended and immobilized, as well as the respective soft adsorption and photolysis are shown in the Figure 9. The best results were achieved in slurry with the use of TiO_2 Degussa P-25, Fe:Ti=0 and Fe:Ti=0.05, with rates of degradation of Cypermethrin 99,84; 99,62; and 100%, respectively. However, the molar ratios higher than Fe:Ti (Fe:Ti=0.075 and Fe:Ti=0.1) had negative effect on the percentage degradation, like what was reported recently by Moradi et al. (2018). in this study, the authors evaluated the photocatalytic degradation of methyl orange (20 mg/L) using TiO_2 doped with different concentrations of Fe^{3+} (0.25, 0.5, 1, 5 and 10 Fe:Ti %mol ratio). These authors found that it is only possible to achieve degradation percentages lower than 5% with the use of catalysts doped with high concentrations of Fe^{3+} (5 to 10 Fe:Ti %mol ratio), which is attributed to the formation of layers composed of iron oxide, photocatalytic reactions generating pollution on the surface of the catalyst particles, which decreases the available active sites, where they occur [57]. For this reason, the authors proposed an acid treatment with HCl (pH 2 solution), to remove impurities that cause inhibition of the photocatalytic activity, achieving a significant improvement in the percentage of degradation.

On the other hand, the phenomenon of inhibition caused by high concentrations of the dopant has also been explained by other authors. Ali et al. (2017), studied the photocatalytic activity of TiO_2 doped with Fe^{3+} ions for the Elimination of methylene blue (10 mg/L), finding high concentrations of dopant (5, 7, and 10 Fe:Ti %mol ratio) produces accumulation on the surface of the catalyst, which reduces the depth of light penetration. In addition, such saturation covers part of the surface of the photosensitive, thus reducing the number of surface active sites for effective degradation of contaminants organic [48].

Based on the results shown in the Figure 9, it can be inferred that the immobilization of nanoparticles on the spathe of coconut palm biomaterial generates a decrease in the percentages of elimination of Cypermethrin, although it is possible to achieve efficiencies of degradation close to 85% for reference Degussa P-25, Fe:Ti=0 and Fe:Ti=0.05, while the doping made with high molar ratios of Fe:Ti (Fe:Ti=0.075 and Fe:Ti=0.1) only allowed to achieve efficiencies of 67 and 48%, respectively; due to above reasons. In addition, there is evidence of the appearance of a yellowish coloration, which is attributed to non-selective degradation of the resin and the biological material used for the immobilization of the powder materials by the hydroxyl radicals generated (OH•) [58].

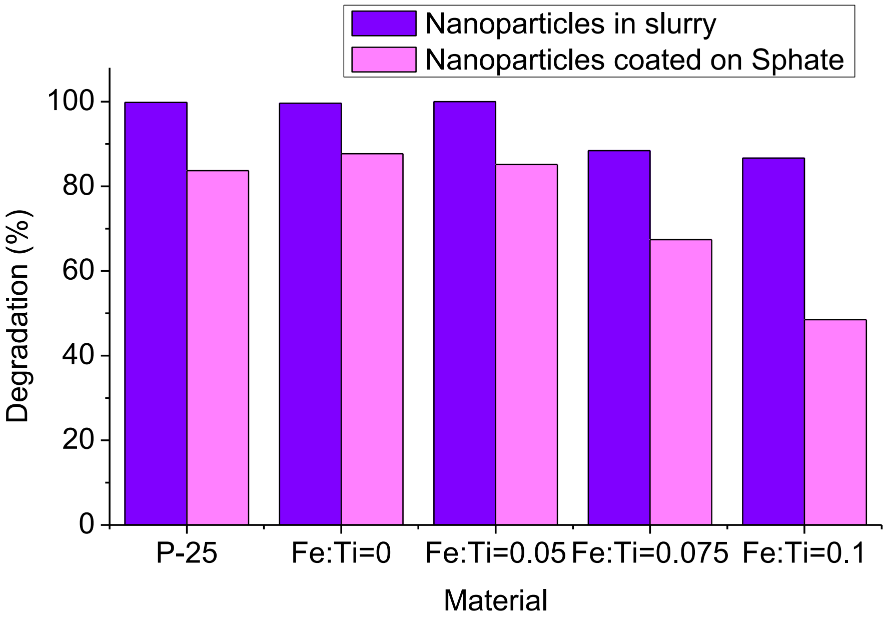

Figure 9. Results for the Cypermethrin solar photocatalytic degradation using GC-MS.

There is also a clear decrease in the efficiency of degradation of the supported systems in comparison to the evaluated in suspension (slurry). Recent studies supporting the low-efficiency catalysts immobilized, which is associated with the substantial decrease in the surface area exposed to the solution, which is much lower than in the case of suspensions. For example, Cerrato et al. (2019) studied the immobilization of TiO_2 on glass materials for the degradation of Ibuprofen under UV-C radiation, finding that the application in suspension allows to achieve the best results for the degradation of the studied drug [59]. Through the Equation (4) the elimination or degradation of Cypermethrin percentages were determined. The results showed values lower than 5% and 10% for the photolysis and dark adsorption tests, respectively; which corresponds to commonly published in research related to targets of molecular adsorption and photolysis of organic compounds, such as pesticides, dyes, and pharmaceuticals, among others [45,60,61].

$$\eta = \frac{(C_0 - C_i)}{C_0} \times 100\% \tag{1}$$

Where, C_0 represents the initial concentration of Cypermethrin in the sample (50 mg/L) and C_f is the concentration at the end of the treatment.

5. Conclusions

The immobilization of nanoparticles on the spathe of coconut palm biomaterial generates a decrease in the percentages of elimination of Cypermethrin, although it is possible to achieve efficiencies of degradation close to 85% for reference Degussa P-25, Fe:Ti=0 and Fe:Ti=0.05, while the doping made with high molar ratios of Fe:Ti (Fe:Ti=0.075 and Fe:Ti=0.1) only allowed to achieve efficiencies of 67 and 48%, respectively. However, the immobilization of nanoparticles on coconut palm-based biomaterial using the resin applied in this study brings two important advantages from an economic and environmental point of view, because it eliminates operating costs associated with the separation of the material after treatment when applied in suspension, and also prevents potential contamination of the effluent treated by nanoparticles TiO_2 or Fe-TiO_2, which could impact negatively on the aquatic ecosystems and human health.

Author Contributions: Preparation and characterization of materials, R.S.; preparation and characterization of materials, R.S.; writing—review and editing, A.H. and R.S.; project administration, A.H.; funding acquisition, A.H.

Funding: This research received no external funding and the APC was funded by University of Cartagena.

Acknowledgments: The authors thank to the University of Cartagena, for its support with Strengthening plan 2017.

Conflicts of Interest: The authors declare no conflict of interest.

References

1. Rani, S. & Sud, D. Role of enhanced solar radiation for degradation of triazophos pesticide in soil matrix. *Sol. Energy* **120**, 494–504 (2015).
2. Cruz, M. *et al.* Bare TiO2 and graphene oxide TiO2 photocatalysts on the degradation of selected pesticides and influence of the water matrix. *Appl. Surf. Sci.* **416**, 1013–1021 (2017).
3. Khan, S. *et al.* Kinetics and mechanism of sulfate radical- and hydroxyl radical-induced degradation of highly chlorinated pesticide lindane in UV/peroxymonosulfate system. *Chem. Eng. J.* **318**, 135–142 (2017).
4. Henych, J. *et al.* Degradation of organophosphorus pesticide parathion methyl on nanostructured titania-iron mixed oxides. *Appl. Surf. Sci.* **344**, 9–16 (2015).
5. Uwizeyimana, H., Wang, M., Chen, W. & Khan, K. The eco-toxic effects of pesticide and heavy metal mixtures towards earthworms in soil. *Environ. Toxicol. Pharmacol.* **55**, 20–29 (2017).
6. García-Mancha, N., Monsalvo, V. M., Puyol, D., Rodriguez, J. J. & Mohedano, A. F. Enhanced anaerobic degradability of highly polluted pesticides-bearing wastewater under thermophilic conditions. *J. Hazard. Mater.* **339**, 320–329 (2017).
7. Hvězdová, M. *et al.* Currently and recently used pesticides in Central European arable soils. *Sci. Total Environ.* **613–614**, 361–370 (2018).
8. Affam, A. C. & Chaudhuri, M. Degradation of pesticides chlorpyrifos, cypermethrin and chlorothalonil in aqueous solution by TiO2 photocatalysis. *J. Environ. Manage.* **130**, 160–165 (2013).
9. Abdennouri, M. *et al.* Photocatalytic degradation of pesticides by titanium dioxide and titanium pillared purified clays. *Arab. J. Chem.* **9**, 313–318 (2016).
10. González-Curbelo, M. Á., Socas-Rodríguez, B., Herrero, M., Herrera-Herrera, A. V. & Hernández-Borges, J. Dissipation kinetics of organophosphorus pesticides in milled toasted maize and wheat flour (gofio) during storage. *Food Chem.* **229**, 854–859 (2017).
11. Shoiful, A., Ueda, Y., Nugroho, R. & Honda, K. Degradation of organochlorine pesticides (OCPs) in water by iron (Fe)-based materials. *J. Water Process Eng.* **11**, 110–117 (2016).
12. World Health Organization. The Who Recommended Classification of Pesticides By Hazard and Guidelines To Classification 2009. *World Heal. Organ.* 1–60 (2010). doi:ISBN 978 92 4 154796 3
13. Ministerio de Proteccion Social Ambiente Desarrollo y Vivienda. *Resolucion número 2115*. *Resolución 2115* 1–23 (2007). doi:10.1017/CBO9781107415324.004

14. Mosleh, S. & Rahimi, M. R. Intensification of abamectin pesticide degradation using the combination of ultrasonic cavitation and visible-light driven photocatalytic process: Synergistic effect and optimization study. *Ultrason. Sonochem.* **35**, 449–457 (2017).
15. Sivagami, K., Vikraman, B., Krishna, R. R. & Swaminathan, T. Chlorpyrifos and Endosulfan degradation studies in an annular slurry photo reactor. *Ecotoxicol. Environ. Saf.* **134**, 327–331 (2016).
16. Sood, S., Umar, A., Mehta, S. K. & Kansal, S. K. Highly effective Fe-doped TiO2nanoparticles photocatalysts for visible-light driven photocatalytic degradation of toxic organic compounds. *J. Colloid Interface Sci.* **450**, 213–223 (2015).
17. Priyanka, K. P., Sankararaman, S., Balakrishna, K. M. & Varghese, T. Enhanced visible light photocatalysis using TiO 2 /phthalocyanine nanocomposites for the degradation of selected industrial dyes. *J. Alloys Compd.* **720**, 541–549 (2017).
18. Liang, H., Jia, Z., Zhang, H., Wang, X. & Wang, J. Photocatalysis oxidation activity regulation of Ag/TiO 2 composites evaluated by the selective oxidation of Rhodamine B. *Appl. Surf. Sci.* **422**, 1–10 (2017).
19. Endo, M. *et al.* Noble metal-modified titania with visible-light activity for the decomposition of microorganisms. *Beilstein J. Nanotechnol.* **9**, 829–841 (2018).
20. Scuderi, V. *et al.* Optical and photocatalytic properties of TiO_2 nanoplumes. *Beilstein J. Nanotechnol.* **8**, 190–195 (2017).
21. Parnicka, P. *et al.* Influence of the preparation method on the photocatalytic activity of Nd-modified TiO_2. *Beilstein J. Nanotechnol.* **9**, 447–459 (2018).
22. Moradi, H., Eshaghi, A., Hosseini, S. R. & Ghani, K. Fabrication of Fe-doped TiO2 nanoparticles and investigation of photocatalytic decolorization of reactive red 198 under visible light irradiation. *Ultrason. Sonochem.* **32**, 314–319 (2016).
23. Wang, Q., Yang, C., Zhang, G., Hu, L. & Wang, P. Photocatalytic Fe-doped TiO2/PSF composite UF membranes: Characterization and performance on BPA removal under visible-light irradiation. *Chem. Eng. J.* **319**, 39–47 (2017).
24. Huo, P. *et al.* Enhanced photodegradation of antibiotics solution under visible light with Fe 2+/Fe 3+ immobilized on TiO 2/fly-ash cenospheres by using ions imprinting technology. *Chem. Eng. J.* **172**, 615–622 (2011).
25. Pazoki, M., Parsa, M. & Farhadpour, R. Removal of the hormones dexamethasone (DXM) by Ag doped on TiO2 photocatalysis. *J. Environ. Chem. Eng.* **4**, 4426–4434 (2016).
26. Zhang, L. *et al.* Electrospun titania nanofibers segregated by graphene oxide for improved visible light photocatalysis. *Appl. Catal. B Environ.* **201**, 470–478 (2017).
27. Márquez Brazón, E., Piccirillo, C., Moreira, I. S. & Castro, P. M. L. Photodegradation of pharmaceutical persistent pollutants using hydroxyapatite-based materials. *J. Environ. Manage.* **182**, 486–495 (2016).
28. Gupta, V. K. *et al.* CoFe2O4@TiO2 decorated reduced graphene oxide nanocomposite for photocatalytic degradation of chlorpyrifos. *J. Mol. Liq.* **208**, 122–129 (2015).
29. Amiri, H. *et al.* Response surface methodology modeling to improve degradation of Chlorpyrifos in agriculture runoff using TiO 2 solar photocatalytic in a raceway pond reactor. *Ecotoxicol. Environ. Saf.* **147**, 919–925 (2018).
30. Yola, M. L., Eren, T. & Atar, N. A novel efficient photocatalyst based on TiO2 nanoparticles involved boron enrichment waste for photocatalytic degradation of atrazine. *Chem. Eng. J.* **250**, 288–294 (2014).
31. Lin, L. *et al.* Degradation of cypermethrin, malathion and dichlorovos in water and on tea leaves with O 3/UV/TiO 2 treatment. *Food Control* **28**, 374–379 (2012).

32. Quiñónes, D. H., Rey, A., Álvarez, P. M., Beltrán, F. J. & Li Puma, G. Boron doped TiO2 catalysts for photocatalytic ozonation of aqueous mixtures of common pesticides: Diuron, o-phenylphenol, MCPA and terbuthylazine. *Appl. Catal. B Environ.* **178**, 74–81 (2014).
33. Maddila, S., Lavanya, P. & Jonnalagadda, S. B. Degradation, mineralization of bromoxynil pesticide by heterogeneous photocatalytic ozonation. *J. Ind. Eng. Chem.* **24**, 333–341 (2015).
34. Solano, R. A., Herrera, A. P., Maestre, D. & Cremades, A. Fe-TiO2 Nanoparticles Synthesized by Green Chemistry for Potential Application in Waste Water Photocatalytic Treatment. *J. Nanotechnol.* **2019**, 1–11 (2019).
35. Balakrishnan, B., Paramasivam, S. & Arulkumar, A. Evaluation of the lemongrass plant (Cymbopogon citratus) extracted in different solvents for antioxidant and antibacterial activity against human pathogens. *Asian Pacific J. Trop. Dis.* **4**, 134–139 (2014).
36. Geetha, T. S. & Geetha, N. Phytochemical screening, quantitative analysis of primary and secondary metabolites of Cymbopogan citratus (DC) stapf. Leaves from Kodaikanal hills, Tamilnadu. *Int. J. PharmTech Res.* **6**, 521–529 (2014).
37. Sundrarajan, M. *et al.* Obtaining titanium dioxide nanoparticles with spherical shape and antimicrobial properties using M. citrifolia leaves extract by hydrothermal method. *J. Photochem. Photobiol. B Biol.* **171**, 117–124 (2017).
38. Birben, N. C. *et al.* Application of Fe-doped TiO2 specimens for the solar photocatalytic degradation of humic acid. *Catal. Today* **281**, 78–84 (2017).
39. Nang Dinh, N., Minh Quyen, N., Chung, D. N., Zikova, M. & Truong, V. Van. Highly-efficient electrochromic performance of nanostructured TiO 2 films made by doctor blade technique. *Sol. Energy Mater. Sol. Cells* **95**, 618–623 (2011).
40. Habibi, M. H. & Habibi, A. H. Photocatalytic degradation of Brilliant Red M5B using four different nanocomposites (ZnFe2O4, porous ZnFe2O4, ZnFe2O4-TiO2, FeTiO3) coated on glass. *J. Ind. Eng. Chem.* **20**, 2964–2968 (2014).
41. Habibi, M. H. & Rahmati, M. H. The effect of operational parameters on the photocatalytic degradation of Congo red organic dye using ZnO-CdS core-shell nano-structure coated on glass by Doctor Blade method. *Spectrochim. Acta - Part A Mol. Biomol. Spectrosc.* **137**, 160–164 (2015).
42. Habibi, M. H. & Rezvani, Z. Photocatalytic degradation of an azo textile dye (C.I. Reactive Red 195 (3BF)) in aqueous solution over copper cobaltite nanocomposite coated on glass by Doctor Blade method. *Spectrochim. Acta - Part A Mol. Biomol. Spectrosc.* **147**, 173–177 (2015).
43. Habibi, M. H. & Parhizkar, J. Cobalt ferrite nano-composite coated on glass by Doctor Blade method for photo-catalytic degradation of an azo textile dye Reactive Red 4: XRD, FESEM and DRS investigations. *Spectrochim. Acta Part A Mol. Biomol. Spectrosc.* **150**, 879–885 (2015).
44. Mejía, M. I., Marín, J. M., Restrepo, G., Pulgarín, C. & Kiwi, J. Photocatalytic evaluation of TiO2/nylon systems prepared at different impregnation times. *Catal. Today* **161**, 15–22 (2011).
45. Lin, L., Wang, H., Jiang, W., Mkaouar, A. R. & Xu, P. Comparison study on photocatalytic oxidation of pharmaceuticals by TiO2-Fe and TiO2-reduced graphene oxide nanocomposites immobilized on optical fibers. *J. Hazard. Mater.* **333**, 162–168 (2017).
46. Soo, C. W., Juan, J. C., Lai, C. W., Hamid, S. B. A. & Yusop, R. M. Fe-doped mesoporous anatase-brookite titania in the solar-light-induced photodegradation of Reactive Black 5 dye. *J. Taiwan Inst. Chem. Eng.* **68**, 153–161 (2016).
47. Yeganeh, M. *et al.* The magnetic characterization of Fe doped TiO2 semiconducting oxide nanoparticles

synthesized by sol–gel method. *Phys. B Condens. Matter* **511**, 89–98 (2017).

48. Ali, T. *et al.* Photocatalytic performance of Fe-doped TiO 2 nanoparticles under visible-light irradiation. *Mater. Res. Express* **4**, 15–22 (2017).
49. Nithya, N., Bhoopathi, G., Magesh, G. & Nesa, C. D. Materials Science in Semiconductor Processing Neodymium doped TiO 2 nanoparticles by sol-gel method for antibacterial and photocatalytic activity. *Mater. Sci. Semicond. Process.* **83**, 70–82 (2018).
50. Haider, A. J., Al-Anbari, R. H., Kadhim, G. R. & Salame, C. T. Exploring potential Environmental applications of TiO2 Nanoparticles. *Energy Procedia* **119**, 332–345 (2017).
51. Hossain, M. K. *et al.* A comparative study on the influence of pure anatase and Degussa-P25 TiO 2 nanomaterials on the structural and optical properties of DSSC photoanode. *Optik (Stuttg).* **171**, 507–516 (2018).
52. Laysandra, L. *et al.* Adsorption and photocatalytic performance of bentonite-titanium dioxide composites for methylene blue and rhodamine B decoloration. *Heliyon* **3**, 1–22 (2017).
53. Liu, Y. *et al.* Fabrication and photovoltaic performance of niobium doped TiO2hierarchical microspheres with exposed {001} facets and high specific surface area. *Appl. Surf. Sci.* **410**, 241–248 (2017).
54. Ganesh, R. S. *et al.* Enhanced photon collection of high surface area carbonate-doped mesoporous TiO2nanospheres in dye sensitized solar cells. *Mater. Res. Bull.* **101**, 353–362 (2018).
55. Wei, J. Q. *et al.* High surface area TiO2/SBA-15 nanocomposites: Synthesis, microstructure and adsorption-enhanced photocatalysis. *Chem. Phys.* **510**, 47–53 (2018).
56. Zayadi, R. A. & Bakar, F. A. Comparative study on the performance of Au/F-TiO2 photocatalyst synthesized from Zamzam water and distilled water under blue light irradiation. *J. Photochem. Photobiol. A Chem.* **346**, 338–350 (2017).
57. Moradi, V., Jun, M. B. G., Blackburn, A. & Herring, R. A. Significant improvement in visible light photocatalytic activity of Fe doped TiO2 using an acid treatment process. *Appl. Surf. Sci.* **427**, 791–799 (2018).
58. Seu, M., Cristina, M. & Ruggeri, W. Selective surface modification of TiO2 -coated polypropylene by photodegradation. *Eur. Polym. J.* **101**, 177–182 (2018).
59. Cerrato, G. *et al.* Micro-TiO2 coated glass surfaces safely abate drugs in surface water. *J. Hazard. Mater.* **363**, 328–334 (2019).
60. Elatmani, K., Ben, N., Plantara, G., Goetz, V. & Ait, I. 3D Photocatalytic media for decontamination of water from pesticides. *Mater. Res. Bull.* **101**, 6–11 (2018).
61. Adeleke, J. T. *et al.* Photocatalytic degradation of methylene blue by ZnO/NiFe2O4 nanoparticles. *Appl. Surf. Sci.* **455**, 195–200 (2018).